Dispersion of the volcanic sulfate cloud from the Mount Pinatubo eruption

Valentina Aquila[1], Luke D. Oman[1], Richard S. Stolarski[1,2], Peter R. Colarco[1], Paul A. Newman[1]

[1] Laboratory for Atmospheric Chemistry and Dynamics, NASA Goddard Space Flight Center, Greenbelt, Maryland, USA

[2] Department of Earth and Planetary Sciences, Johns Hopkins University, Baltimore, MD, USA

Abstract

We simulate the transport of the volcanic cloud from the 1991 eruption of Mount Pinatubo with the GEOS-5 general circulation model. Our simulations are in good agreement with observational data. We tested the importance of initial condition corresponding to the specific meteorological situation at the time of the eruption by employing reanalysis from MERRA. We found no significant difference in the transport of the cloud. We show how the inclusion of the interaction between volcanic sulfate aerosol and radiation is essential for a reliable simulation of the transport of the volcanic cloud. The absorption of long wave radiation by the volcanic sulfate induces a rising of the volcanic cloud up to the middle stratosphere, combined with divergent motion from the latitude of the eruption to the tropics. Our simulations indicate that the cloud diffuses to the northern hemisphere through a lower stratospheric pathway, and to mid- and high latitudes of the southern hemisphere through a middle stratospheric pathway, centered at about 30 hPa. The direction of the middle stratospheric pathway depends on the season. We did not detect any significant change of the mixing between tropics and mid- and high latitudes in the southern hemisphere.

1. Introduction

Volcanic eruptions are a major source of stratospheric aerosol [*Deshler*, 2008]. Sulfur dioxide injected into the stratosphere by large eruptions is oxidized into sulfate aerosol and can increase the background aerosol mass by orders of magnitude. The induced perturbation of the stratospheric aerosol layer can persist for some years. During such

time the aerosol can spread over the whole globe, changing the global climate in a significant way [*Robock*, 2000].

Mt. Pinatubo is located in the Philippines (15.1°N, 120.4°E). Pinatubo erupted on June 15th, 1991, injecting about 20 Tg of sulfur dioxide into the atmosphere [*Bluth et al.*, 1992]. The resulting sulfate cloud was detected at altitudes higher than 30 km [*McCormick and Veiga*, 1992] and, after about one year, roughly one third of the volcanic aerosol was still present in the atmosphere.

The sulfate cloud generated by the eruption of Mt. Pinatubo circled around the Earth within 3 weeks of the eruption [*Guo et al.*, 2004; *McCormick and Veiga*, 1992], crossing the equator and diffusing to mid- and high latitudes in both the northern and the southern hemispheres.

Such a broad meridional spreading of the cloud is not typical of all tropical eruptions. For example, the cloud from the June 1982 El Chichón eruption, which is located 2° north of Mt. Pinatubo, was mainly confined to the northern hemisphere [*McCormick and Swissler*, 1983]. *Young et al.*, [1994] first suggested that the cross-equatorial transport of the Mt. Pinatubo cloud was due to local absorption of infrared radiation from the troposphere. *Timmreck et al.*, [1999a] confirmed this hypothesis from a theoretical point of view with a one-simulation study with the MAECHAM4 Hamburg climate model.

Niemeier et al., [2009] applied the most recent version of the MAECHAM5 Hamburg climate model, coupled to an aerosol microphysical model, to the study of the Pinatubo eruption. Other studies, such as *Stenchikov et al.*, [1998], *Kirchner et al.*, [1999] and *Thomas et al.*, [2009a; 2009b] used prescribed aerosol distributions.

55 It is still unclear if the eruption of Mt. Pinatubo modified the circulation in the
56 southern hemisphere. *Robock et al.*, [2007] identified no significant anomaly in the
57 southern hemisphere circulation in their simulations with the NASA/GISS ModelE
58 general circulation model. In contrast, *Karpechko et al.*, [2010], *Marshall*, [2003], *Roscoe*
59 *and Haigh*, [2007] and *Crooks and Gray*, [2005] found a negative response of the
60 Southern Annular Mode in both models and observations.

61 In this paper, we simulate the eruption of Mt. Pinatubo and the dispersal of the
62 subsequent sulfate cloud with the Goddard Earth Observing System (GEOS-5) general
63 circulation model [*Rienecker et al.*, 2008], coupled to the GOCART aerosol transport
64 module [*Colarco et al.*, 2010] and the StratChem stratospheric chemistry module
65 [*Pawson et al.*, 2008]. GEOS-5 is here for the first time applied to the simulation of
66 stratospheric volcanic aerosol.

67 In section 2, we describe the model and the modifications introduced to simulate
68 stratospheric volcanic aerosol. Given the large amount of observations, the eruption of
69 Mt. Pinatubo is a good test for the ability of GEOS-5 to correctly simulate the dispersal
70 of the volcanic cloud and the response to sudden aerosol perturbations in the stratosphere.

71 In section 3, we present the model results and the comparison with observations.
72 We show that our simulations are in good agreement with observations.

73 Finally, in section 4 we apply GEOS-5 to the study of the interaction between Mt.
74 Pinatubo aerosols and the stratospheric circulation, focusing on the mixing between
75 tropics and midlatitudes.

2. The GEOS-5 general circulation model

All simulations presented in this study are performed with the Goddard Earth Observing System, Version 5 (GEOS-5) model [*Rienecker et al.*, 2008], a system of component models integrated using the Earth System Modeling Framework (ESMF).

The GEOS-5 atmospheric general circulation model (AGCM) is able to perform weather and climate simulations used for atmospheric analyses, weather forecasts and climate simulations and predictions. GEOS-5 uses a finite-volume dynamical core [*Lin*, 2004] combined with a physics package that describes moist processes, radiation, turbulent mixing and surface processes.

The convective parameterization Relaxed Arakawa-Schubert (RAS) is described by *Moorthi and Suarez*, [1992], and is combined to a prognostic cloud scheme. The boundary-layer turbulent mixing is parameterized with the schemes by *Louis et al.*, [1982] and *Lock et al.*, [2000], for stable and unstable situations, respectively. The land-surface model is composed of a catchment-based hydrological model [*Koster et al.*, 2000] and by a multi-layer snow model [*Stieglitz et al.*, 2001]. Coupled chemistry-climate simulations can be performed using the StratChem module for stratospheric chemistry [*Pawson et al.*, 2008].

The radiative transfer model consists of a solar radiation model [*Chou and Suarez*, 1999] and a thermal radiation model [*Chou et al.*, 2001]. The solar radiation model includes absorption due to water vapor, O_3, O_2, CO_2, clouds and aerosol. The thermal radiation model includes absorption by water vapor, CO_2, O_3 and most of the minor trace gases, as well as clouds and aerosol.

99 The aerosol optical properties are read from look-up tables previously generated
100 using the OPAC database [*Hess et al.*, 1998]. The look-up tables contain the aerosol mass
101 scattering and extinction coefficients as a function of relative humidity and radiation
102 wavelength. We apply the Mie theory to calculate of the aerosol optical properties, and
103 assume that aerosol is log-normally distributed and externally mixed.

104 GEOS-5 can be run both in climate or data assimilation mode. The simulations
105 performed in this study are climate mode simulations, i.e. they provide a forecast of the
106 climate starting from specified initial conditions. We apply GEOS-5 with resolution 2.0°
107 x 2.5° latitude by longitude. The model has 72 vertical layers in a hybrid coordinate
108 system from surface to 0.01 hPa.

109 The aerosol transport model in the GEOS-5 AGCM is based on the Goddard
110 Chemistry, Aerosol, Radiation and Transport (GOCART) model [*Chin et al.*, 2000;
111 2002]. An online version of GOCART in GEOS-4, a previous version of GEOS-5, has
112 been validated by *Colarco et al.*, [2010]. Versions of GOCART in GEOS-5 have been
113 already used in several recent field campaigns, as TC4 (2007), ARCTAS (2008) and
114 GloPac (2010).

115 The aerosol species treated by GOCART as described in *Colarco et al.*, [2010]
116 are dust, sea salt, black carbon, organic carbon and sulfate (SO_4). In this study, only the
117 sulfate component is active. GOCART includes a parameterization of the chemical
118 production of SO_4 from oxidation of dimethyl sulfide (DMS) by OH during day and NO_3
119 during night, and from oxidation of sulfur dioxide (SO_2) by OH in the gas phase and by
120 H_2O_2 in the aqueous phase.

GEOS-5 can run with radiatively interactive aerosol, which means that the aerosol concentrations simulated by GOCART can modify the meteorological fields. The simulations shown in Section 4 are performed with radiatively interactive aerosol. Some results from runs with non-interactive aerosol are presented in Section 4.

We introduced a parameterization of the settling of SO_4 to properly simulate stratospheric volcanic aerosol. The settling velocity is a function of the particle's wet radius. The sulfate growth factor β_{SO4} is calculated as a function of the relative humidity RH following *Petters and Kreidenweis*, [2007] as

$$\beta_{SO_4} = \frac{r_{wet}}{r_{dry}} = \sqrt[3]{\frac{RH(1-k)-1}{RH-1}},$$

where the hygroscopic parameter k is equal to 1.19 and r_{dry} the dry effective radius, which is a tuning parameter.

Assuming a lognormal distribution, the modal radius r_m and the effective radius r_e are related through the equation

$$r_e = r_m \exp\left[\frac{5}{2}\ln^2\sigma\right],$$

where σ is the standard deviation of the distribution.

We performed several sensitivity tests varying the value of the sulfate dry radius. In this work we assume that aerosol is lognormal distributed with median diameter radius to 0.35 μm and standard deviation 1.25. This corresponds to an effective dry radius equal to 0.40 μm. This modal radius is within the range of observed values for sulfate aerosol from Mt. Pinatubo (e.g. *Bingen et al.*, [2004]; *Niemeier et al.*, [2009]; *Russell et al.*,

141 [1996]; *Stenchikov et al.*, [1998]), and result in good agreement with the AOT retrieved
142 by SAGE-II and AVHRR (Section 3). The simulated *e*-folding time for sulfate is about
143 one year (Table 1), as the one calculated from observations [*McCormick et al.*, 1995].

144 3. Simulation of the Mt. Pinatubo eruption

145 We simulated the eruption of Mt. Pinatubo by injecting 20 Tg of sulfur dioxide in the
146 grid box containing Mt. Pinatubo during the day of June 15th, 1991. The SO_2 load is
147 initially distributed between 16 km and 18 km, and is lofted to higher altitudes within the
148 first weeks due to the model response to radiatively interacting aerosol.

149 Other model studies, as e.g. [*Timmreck et al.*, 1999b] and [*Zhao et al.*, 1995],
150 place the injection of SO_2 at higher altitude. They base their assumption on SAGE-II
151 observations. At the moment of the eruption, however, SAGE-II was observing at about
152 70°N [*Trepte et al.*, 1993], and observed at the latitude of Mt. Pinatubo only 15 days after
153 the eruption. At that stage the absorption of radiation by the volcanic aerosol had already
154 induce the lofting of the cloud itself.

155 We tested similar assumptions on the injection height in GEOS-5 by performing
156 simulations with injection of SO_2 between 16 km and 25 km, 17 km and 27 km, 20 km
157 and 27 km, 20 km and 30 km. In all these simulations, the bulk of the volcanic cloud
158 reached altitudes much higher than observations. Our choice of a lower injection altitude
159 results in a reasonable simulation of the SAGE-II vertical profile after a couple of weeks
160 from the day of the eruption (Section 3.2).

161 We did not include any other aerosol sources in the simulations used for this
162 work.

163 We performed an ensemble of eight transient simulations, each spanning from
164 January 1991 to December 1997. The initial conditions of the ensemble members are the
165 meteorological fields of eight different Januaries of a control simulation with no volcanic
166 perturbation, which was initialized with climatological meteorological fields typical of
167 the year 2000.

168 The injected SO_2 is transformed into SO_4 by GOCART with an average *e*-folding
169 time of 29.8 days, in good agreement with observations by the Total Ozone Mapping
170 Spectrometer (TOMS) [*Bluth et al.*, 1992; *Guo et al.*, 2004]. The average of the SO_4 *e*-
171 folding times of the eight ensemble members is 347 days with a standard deviation of
172 57.7 days, also in good agreement with observations [*Barnes and Hofmann*, 1997; *Nagai*
173 *et al.*, 2010]. Table 1 shows the *e*-folding times of SO_2 and SO_4 for each ensemble
174 member.

175 Figure 1 shows the temporal evolution of the globally averaged AOT at 550 nm.
176 The results from our simulations are compared to SAGE II [*Thomason et al.*, 1997] and
177 AVHRR [*Long and Stowe*, 1994] observations. We removed background values from the
178 AVHRR observations, calculated as the monthly mean AOT over the available months
179 preceeding the eruption (June 1989 to May 1991).

180 The simulated peak value is in reasonable agreement with AVHRR, but is higher
181 in magnitude and occur earlier in time than the SAGE-II data. Optical depths of about
182 0.15 or more, however, saturate the SAGE-II measurement [*Russell et al.*, 1996]. Hence,
183 the value of AOT calculated from SAGE-II observations are likely underestimated.
184 Additionally, the sampling of SAGE-II observations is relatively sparse and can hardly

185 register rapid changes in the AOT. After January 1992 both SAGE-II and AVHRR
186 observations are within the variability of the ensemble.

187 3.1. Horizontal dispersion of the volcanic cloud

188 Shortly after the eruption, the volcanic cloud is transported northward out of the tropics
189 and southward toward the equator.

190 Figure 2 shows the zonal mean of the AOT as a function of time in our
191 simulations and in the satellite observations. The model reproduces reasonably well the
192 spreading of the cloud into the two hemispheres observed by SAGE-II and AVHRR.
193 GEOS-5 simulates well the timing and the intensity of the tropical peak compared to
194 AVHRR. As expected from the profiles in Figure 1, the magnitude of the simulated
195 aerosol optical thickness is larger than the one observed by SAGE-II.

196 GEOS-5 simulates also the second peak in February, 1992 at 45°N, as well as the
197 secondary peak detected by AVHRR at about 10°N in September, 1991. The high AOT
198 values observed at 60°S in November 1991 might be due to the eruption of the Cerro
199 Hudson volcano (72.97°W, 45.90°S) between August and October 1991, which is not
200 included in our simulations.

201 GEOS-5 transports a large fraction of the cloud southward shortly after the
202 eruption, but slightly underestimates the transport across the equator with respect to the
203 observations. While the simulated peak is located on the equator, both SAGE-II and
204 AVHRR detected the peak at about 5°S. The results by [*Timmreck et al.*, 1999a] also
205 underestimated the cross-equatorial transport. They suggested that the missing transport

might be due to the specific synoptic situation in June 1991, when a strong high over Tibet induced a southward transport of the cloud.

We tested the importance of the specific meteorological situation by performing a simulation with specified initial conditions from the Modern Era Retrospective Analyses (MERRA, *Rienecker et al.*, [2011]). The results (not shown) are similar to the one of the reference simulations, with a peak of the AOT on the equator. This suggest that the particular meteorological situation at the moment of the eruption is not responsible for the additional southward transport.

The tests performed with different injection heights (Section 3) showed a very similar horizontal distribution of the AOT, even if the volcanic clouds reached altitudes higher than observed.

The small initial underestimation of the southward transport might be due to the lack of a radiatively interactive SO_2 in the version of GEOS-5 used in this work. *Lary et al.*, [1994] estimated that the SO_2 heating rate can be up to 1 K/day and could therefore be significant in the early stages of the cloud's evolution.

3.2. Vertical distribution of the volcanic cloud

We compare our results with SO_2 profiles taken with a microwave limb sounder (MLS) by *Read et al.*, [1993] between 10°S and the equator on September 21st, 1991 (Figure 3). The simulated profiles correspond to the September 1991 monthly mean of the SO_2 vertical profiles, averaged over the latitudinal band between 10°S and 10°N. We averaged over a latitudinal band larger than the MLS observations to take into account the different transport pattern between simulations and observations.

228 The agreement with [*Read et al.*, 1993] is good: both SO_2 profiles have a peak at
229 about 20 hPa of similar magnitude. The sensitivity tests that we performed varying the
230 injection altitude of SO_2 showed differences in the vertical profile of the volcanic cloud
231 during the first months, but the equilibrium level where the bulk of the cloud settles was
232 in all tests at about 20 hPa.

233 Figure 4 shows the vertical distribution of the zonally averaged SO_4 concentration
234 on July 15th, September 1st, November 1st and December 31st, 1991. The bulk of the cloud
235 is between 50 hPa and 10 hPa in July 1991.

236 The model results are in agreement with SAGE-II observational satellite data,
237 which detected the cloud top at altitudes up to 29 km (about 10 hPa) during June, July
238 and August 1991 [*McCormick and Veiga*, 1992].

239 *Trepte et al.*, [1993] showed the latitude-altitude cross-section of the SAGE-II 1
240 μm extinction ratio. Data were first collected in the tropical region between July 1st and
241 July 20th, and show values higher than the background between the tropopause and 30 km
242 altitude, in reasonable agreement with the first panel of Figure 4.

243 The simulated vertical profiles for December (Figure 4, lower-right panel) also
244 agrees with SAGE-II data, as analyzed by *Vernier et al.*, [2011]. They detected the
245 volcanic cloud at altitudes higher than 35 km, with its bulk between 26 and 27 km.

246 3.3. Cross-equatorial transport

247 The volcanic cloud moves to mid- and high latitudes through two main transport
248 pathways, as shown in Figure 4. Already one week after the eruption, part of the cloud is

advected northward through the lower stratosphere at about 100 hPa. A portion of the cloud, instead, later reaches southern higher latitudes through the middle stratosphere between 5 and 50 hPa and arrives at 90°S in the middle of November (Figure 4, lower panels).

The volcanic cloud crosses the equator during the first two weeks after the eruption, but the transport from the tropics to southern midlatitudes does not start until the middle of July and becomes significant in September (Figure 4, upper right panel).

The middle stratospheric transport regime is illustrated in Figure 5. In our simulations the volcanic cloud reaches 30 hPa about one week after the eruption (not shown) and is by then still located in the northern hemisphere. At the same time part of the cloud has already reached 40°N and 30°S latitude through the lower stratospheric pathway. At the beginning of July (Figure 5, upper panel) the volcanic cloud has dispersed longitudinally over nearly the whole globe, but is still confined in the tropical area, with a sharp gradient at 20°S. The same configuration was observed in SAGE-II data [*McCormick and Veiga*, 1992; *Trepte et al.*, 1993].

About one month after the eruption we observe the first intrusion of volcanic material from the southern tropics to midlatitudes through tongue-like structures that appear in the middle stratosphere (Figure 5, lower panel). Such tongues of air have been identified by *Randel et al.*, [1993] as the path of mixing from the tropics to midlatitudes. *Trepte et al.*, [1993] detected in the SAGE-II observations similar intrusions detaching from the tropical cloud at 20°S between July 11th, 1991 and July 18th, 1991.

Our transport simulation of the volcanic cloud from the Mt. Pinatubo eruption is in good agreement with the observations. Both the vertical and horizontal distribution and

272 the timing of the mixing to mid- and high latitudes are reasonably well comparable to
273 SAGE-II and AVHRR observations.

274 4. Importance of a radiative active volcanic aerosol

275 We investigate how the interaction between volcanic aerosol from Mt. Pinatubo and
276 radiation changed the background mixing within the tropics and from the tropics to
277 midlatitudes. We performed an ensemble of simulations with no interactive aerosol, and
278 compared them to the reference simulation of the dispersal of the volcanic cloud
279 evaluated in Section 3. We performed one additional ensemble of eight members without
280 coupling between aerosol and radiation. Each ensemble member has exactly the same
281 setup of the reference simulations.

282 Figure 6 (upper panel) shows the temporal evolution of the zonally averaged AOT
283 at 550 nm, to be compared to the upper panel of Figure 2. In the non-interactive
284 ensemble, most of the volcanic cloud is directed toward the northern hemisphere, faster
285 than in the reference simulation. This is due to the different vertical distribution of the
286 volcanic cloud: in the non-interactive case the volcanic cloud stays at much lower
287 altitudes (Figure 7, middle panel) than in the interactive case (Figure 7, left panel).
288 Hence, the non-interactive cloud does not rise enough to enter the middle stratosphere,
289 and the advection of the cloud to midlatitudes takes place only through the lower
290 stratosphere. The *e*-folding time of SO_4 is much lower in the ensemble with non-
291 interactive aerosol than in the reference case (74 days against 346 days).

292 We also performed an ensemble of three non-interactive simulations directly
293 injecting SO_2 between 17 km - 27 km (Figure 6, lower panel). Also in this case the cross-

294 equatorial transport is not as intense as in the reference simulation, and the volcanic cloud
295 looks even more confined to the tropics than in Figure 6a. Even if the SO_4 cloud reaches
296 the middle stratosphere (Figure 7, right panel) and part of the cloud crosses the equator, it
297 remains confined within the tropics.

298 The additional transport to the southern hemisphere is therefore due to the
299 radiative interaction of volcanic aerosol, and is essential for a good simulation of the
300 dispersal of the volcanic cloud, as observed by *Timmreck et al.*, [1999a].

301 4.1. Perturbation of the background winds

302 In Figure 8 we show the perturbation of the horizontal wind fields induced by the
303 interaction between radiation and volcanic aerosol. We show the difference of the
304 horizontal winds between the interactive and the non-interactive ensembles on June 16th,
305 1991 at 70 hPa and on July 1st, 1991, together with the aerosol heating rates due to
306 longwave radiation. To reduce noise effects, the results for July 1st in Figure 8 and Figure
307 10 are from an eight-member ensemble of non-interactive simulations starting on the
308 midnight of July 1st, with initial conditions from July 1st of the interactive run.

309 The sudden warming generates a divergent motion from the location of the
310 volcanic cloud already one day after the eruption (Figure 8, upper panel). The simulated
311 volcanic cloud is still at the same latitude as Mt. Pinatubo, and has not risen yet to
312 altitudes higher than 50 hPa. On July 1st (Figure 8, lower panel) the cloud has circled
313 nearly around the whole globe, but, in the middle stratosphere, is still confined between
314 20°S and 20°N.

315 The perturbation of the horizontal winds diffuses the sulfate northward and
316 southward from the center of the clouds, increasing the spreading of the clouds towards
317 the tropics, due to the heating induced by the SO_4 absorption of longwave radiation. The
318 winds are no longer significantly perturbed at 30 hPa by December 1991, when the
319 concentration of SO_4 becomes meridionally homogeneous. At 50 hPa, where the SO_4
320 concentration decreases (Figure 4), the winds converge towards the center of the cloud.
321 At altitudes lower than 50 hPa no consistent perturbation is simulated.

322 GEOS-5 simulates the formation of two vortices at the location of the volcanic
323 cloud during the second week after the eruption, north and south of the equator,
324 respectively (Figure 9). This feature is similar to the response to a tropical tropospheric
325 heating source calculated by [*Gill*, 1980], with a high pressure system at the top of the
326 perturbation and a low pressure one at the bottom. A comparison with observation could
327 identify if such a response was indeed observed.

328 The divergent winds are strongly related to an increased upwelling. Figure 10
329 shows the perturbation of the wind's vertical velocity on the same days and levels
330 depicted in Figure 8, and the contours of the SO_4 distribution. The increase of the vertical
331 velocity is significant: in the non-interactive case the values of the vertical velocity are up
332 to 0.5 mm/s, while in the perturbed case they reach up to 4 mm/s, in the regions with
333 highest concentration of sulfate. In some regions the perturbation even changes the sign
334 of the vertical wind.

335 The absorption of longwave radiation by volcanic SO_4 is responsible for the "self-
336 lofting" of the volcanic clouds and for the divergent motion from the areas with highest
337 SO_4 concentration. As already mentioned in Section 3.1, the introduction of radiative

338 interactive SO_2 could possibly increase the lofting and spreading of the cloud during the
339 first months from the eruption.

340 The first stage of the volcanic cloud's transport to the southern hemisphere is
341 driven by the absorption of longwave radiation and comprises the transport from the
342 latitude of the eruption across the equator and to the tropics.

343 Afterwards, the cloud is transported from the tropics to southern mid- and high
344 latitudes through the structures depicted in Figure 5. We investigated if the volcanic
345 perturbation from Mt. Pinatubo enhanced such structures, and hence the mixing between
346 tropics and midlatitudes, by analyzing the distribution of N_2O (not shown).

347 Climatologically, the concentration of N_2O is highest in the tropics and presents a
348 strong summer gradient between the tropics and midlatitudes. The sources of N_2O are
349 located at surface and its concentration decreases with altitude.

350 Compared to the unperturbed case, GEOS-5 simulates decreased N_2O at about 30
351 hPa and increased N_2O at 10 hPa in the tropical region starting from September 1991,
352 compatible with the lofting of air induced by the volcanic perturbation. The effect of the
353 lofting weakens starting from January 1992 and no significant change in the N_2O
354 concentration can be detected after September 1992.

355 There is no sign of increased N_2O transport from the tropics to midlatitudes.

356 The analysis of the age of air at 30 hPa leads to similar conclusion (not shown).
357 The air in the interactive runs is younger in the tropical area between July and December
358 1991, implying a faster upwelling, but there is no significant difference in the following
359 months, neither in the tropics nor at midlatitudes.

4.2. Impact of the sulfate burden on the spreading of the volcanic cloud

We performed two interactive experiments lowering the amount of injected SO_2 to 5 Tg. In the first experiment we injected SO_2 between 16 km and 18 km, in the second between 17 km and 27 km. The set up of the simulations is otherwise identical to the reference simulation. Figure 11 shows the vertical profiles of the zonal mean of SO_4 in the two experiments.

In the experiment with low injection height (Figure 11a) the volcanic cloud is mainly confined to the lower stratosphere, showing that 5 Tg of SO_2 do not produce a strong enough perturbation to raise the cloud to the middle stratosphere.

In the second experiment (Figure 11b) the cloud is injected already in the middle stratosphere and is advected to the southern hemisphere through the same middle stratospheric pathway as in the reference simulation. However, the peak of SO_4 is north of the equator, while in the reference simulation it's partly in the southern hemisphere already on July 15th (Figure 4).

The cross-equatorial transport is slower in the experiment with low burden. The outer edges of the cloud cross the equator in August 1991 and diffuse outside the tropical area starting from October 1991, compared to the end of June 1991 and August 1991, respectively, of the reference simulation.

A lower injected sulfate burden generates a less intense perturbation, which, however, eventually produces the same transport pattern as in the reference case, when the SO_2 is injected at a higher altitude. Hence, the perturbation induced by the injection

382 of 5 Tg of sulfate is not strong enough to bring the cloud to the middle stratosphere but, if
383 directly injected at that altitude, such perturbation is sufficient to push the cloud south of
384 the equator and to midlatitudes.

385 4.3. Seasonality of the cross-equatorial transport

386 The cross-equatorial transport is related to the season of the eruption. We performed two
387 experiments injecting 20 Tg of SO_2 in winter (January 15th) and in spring (April 4th, day
388 of the 1982 eruption of El Chichón). The setup of the experiments was otherwise
389 identical to the reference simulation.

390 In the first experiment the volcanic cloud stays mainly in the northern
391 hemisphere, even if reaches the same altitude as in the reference experiment. The peak of
392 SO_4 concentration is in the northern hemisphere between 10°N and 30°N in February, and
393 during the following four months the cloud extends across the equator. The middle
394 stratospheric pathway is present also in this simulation, but is directed towards northern
395 high latitudes. It is not until June that a small amount of sulfate crosses 30°S and reaches
396 the southern midlatitudes through the same middle stratospheric pathway.

397 In the springtime injection experiment the peak of sulfate aerosol also stays in the
398 northern hemisphere, between 0 and 10°N. The edge of the cloud crosses the equator
399 already during the first month, and start spreading to midlatitudes in June. As in the
400 reference simulation, a considerable fraction of the cloud is directed to southern
401 midlatitudes through the middle stratospheric pathway. The seasonality of the mixing
402 alone, therefore, does not appear to be responsible for the different transport pattern of
403 the El Chichón and Mt. Pinatubo volcanic cloud.

5. Conclusions

Our GEOS-5 simulations of the transport of the volcanic cloud from the Mt. Pinatubo's eruption are in good agreement with observations. Our simulations show that including interaction between radiation and volcanic SO_4 is essential to properly simulate the impact of volcanoes on the atmospheric circulation, as initially suggested by *Young et al.*, [1994] and *Fairlie*, [1995].

The aerosol volcanic cloud diffuses across the globe through two main pathways: one pathway is centered in the lower stratosphere, at about 100 hPa, while the other is centered in the middle stratosphere. The volcanic cloud of Mt. Pinatubo diffuses to the northern hemisphere mainly in the lower stratosphere and to the southern hemisphere in the middle stratosphere.

We can divide the transport problem of the Pinatubo aerosol to the southern hemisphere in two stages: During the first stage, the absorption of longwave radiation from the cloud induces a lofting and a divergent motion from the center of the cloud. The self-induced transport of the cloud pushes the aerosol northward and southwards across the equator and to the tropics. The magnitude of the perturbation of the vertical velocity is closely related to the distribution of volcanic SO_4 and causes significant perturbations of the tropical circulation until December 1991.

The second stage, starting from about one month after the eruption, includes the transport from 30°S to southern mid- and high latitudes. Such transport takes place through tongue-like structures, which are the common way of mixing between the tropics and midlatitudes [*Randel et al.*, 1993]. Analyzing the horizontal distribution of N_2O, we

426 could not detect any significant enhancement of the mixing between tropics and
427 midlatitudes.

428 The transport across the equator is strongly dependent on the season and is much
429 enhanced during the southern hemispheric winter. The seasonal dependence of the
430 transport, however, does not appear to be responsible for the different transport pattern of
431 the volcanic cloud from Mt. Pinatubo and El Chichón. Our simulations suggest that the
432 different transport might be rather related to the amount of SO_2 injected in the
433 atmosphere. An injected burden equal to 5 Tg SO_2 is not sufficient in our simulation to
434 take the volcanic cloud to the middle stratosphere. El Chichón injected about 7 Tg of SO_2
435 in the atmosphere [*Bluth et al.*, 1992], which might as well have not been enough to
436 induce lofting to the middle stratosphere.

437 **Acknowledgments**

438 We thank Anne Douglass, Steven Pawson and Chaim Garfinkel for helpful discussions.
439 V. Aquila is supported by the NASA Postdoctoral Program, administered by the Oak
440 Ridge Associated University (ORAU).

441

441

442 References

443

444 Barnes, J. E., and D. J. Hofmann (1997), Lidar measurements of stratospheric aerosol
445 over Mauna Loa Observatory, *Geophys Res Lett*, *24*(15), 1923–1926.

446 Bingen, C., D. Fussen, and F. Vanhellemont (2004), A global climatology of
447 stratospheric aerosol size distribution parameters derived from SAGE II data over the
448 period 1984-2000: 1. Methodology and climatological observations, *J Geophys Res-*
449 *Atmos*, *109*(D6), D06201, doi:10.1029/2003JD003518.

450 Bluth, G. J. S., S. D. Doiron, C. C. Schnetzler, A. J. Krueger, and L. S. Walter
451 (1992), Global tracking of the SO_2 cloud from the June, 1991 Mount Pinatubo
452 eruptions, *Geophys Res Lett*, *19*(2), 151–154.

453 Chin, M., R. B. Rood, S.-J. Lin, and J.-F. Müller (2000), Atmospheric sulfur cycle
454 simulated in the global model GOCART: Model description and global properties, *J.*
455 *Geophys. Res.*, *105*(D20), 24671–24687, doi:10.1029/2000JD900384.

456 Chin, M., P. Ginoux, S. Kinne, O. Torres, B. Holben, B. Duncan, R. Martin, J.
457 Logan, A. Higurashi, and T. Nakajima (2002), Tropospheric aerosol optical thickness
458 from the GOCART model and comparisons with satellite and Sun photometer
459 measurements, *J Atmos Sci*, *59*(3), 461–483.

460 Chou, M.-D., M. J. Suarez, X.-Z. Liang, and M. M.-H. Yan (2001), *A Thermal*

461 *Infrared Radiation Parameterization for Atmospheric Studies*, NASA.

462 Chou, M.-D., and M. J. Suarez (1999), *A solar radiation parameterization for*
463 *atmospheric studies*, Technical report series on global modeling and data
464 assimilation, M. J. Suarezedited by, NASA.

465 Colarco, P., A. Da Silva, M. Chin, and T. Diehl (2010), Online simulations of global
466 aerosol distributions in the NASA GEOS-4 model and comparisons to satellite and
467 ground-based aerosol optical depth, *J. Geophys. Res.*, *115*(D14), D14207,
468 doi:10.1029/2009JD012820.

469 Crooks, S. A., and L. J. Gray (2005), Characterization of the 11-Year Solar Signal
470 Using a Multiple Regression Analysis of the ERA-40 Dataset, *J. Clim.*, *18*, 996–
471 1015, doi:10.1175/JCLI-3308.1.

472 Deshler, T. (2008), A review of global stratospheric aerosol: Measurements,
473 importance, life cycle, and local stratospheric aerosol, *Atmos Res*, *90*(2-4), 223–232,
474 doi:10.1016/j.atmosres.2008.03.016.

475 Fairlie, T. (1995), Three-dimensional transport simulations of the dispersal of
476 volcanic aerosol from Mount Pinatubo, *QJR Meteorol. SOC.*

477 Gill, A. E. (1980), Some simple solutions for heat-induced tropical circulation,
478 *Quart. J. R. Met. Soc.*, *106*(449), 447–462, doi:10.1002/qj.49710644905.

479 Guo, S., G. BLUTH, W. Rose, I. Watson, and A. Prata (2004), Re-evaluation of SO2
480 release of the 15 June 1991 Pinatubo eruption using ultraviolet and infrared satellite

481 sensors, *Geochem Geophy Geosy*, *5*, –, doi:10.1029/2003GC000654.

482 Hess, M., P. Koepke, and I. Schult (1998), Optical properties of aerosols and clouds:
483 The software package OPAC, *B Am Meteorol Soc*, *79*(5), 831–844.

484 Karpechko, A. Y., N. P. Gillett, M. Dall'Amico, and L. J. Gray (2010), Southern
485 Hemisphere atmospheric circulation response to the El Chichón and Pinatubo
486 eruptions in coupled climate models, *Q J Roy Meteor Soc*, *136*(652), 1813–1822,
487 doi:10.1002/qj.683.

488 Kirchner, I., G. L. Stenchikov, H.-F. Graf, A. Robock, and J. C. Antuña (1999),
489 Climate model simulation of winter warming and summer cooling following the
490 1991 Mount Pinatubo volcanic eruption, *J. Geophys. Res.*, *104*(D16), 19039–19055,
491 doi:10.1029/1999JD900213.

492 Koster, R. D., M. J. Suarez, A. Ducharne, M. Stieglitz, and P. Kumar (2000), A
493 catchment-based approach to modeling land surface processes in a general circulation
494 model 1. Model structure, *J. Geophys. Res.*, *105*, D20, doi:10.1029/2000JD900327.

495 Lary, J. D., M. Balluch, and S. Bekki (1994), Solar heating rates after a volcanic
496 eruption: The importance of SO_2 absorption, *Q. J. R. Meteorol. Soc*, *120*, 1683–1688.

497 Lin, S.-J. (2004), A "vertically lagrangian" finite-volume dynamical core for global
498 models, *Mon. Wea. Rev.*, *132*, 2293–2307, doi:10.1175/1520-
499 0493(2004)132<2293:AVLFDC>2.0.CO;2.

500 Lock, A. P., A. R. Brown, M. R. Bush, G. M. Martin, and R. N. B. Smith (2000), A

501 New Boundary Layer Mixing Scheme. Part I: Scheme Description and Single-
502 Column Model Tests, *Mon. Wea. Rev.*, *128*, 3187–3199, doi:10.1175/1520-
503 0493(2000)128<3187:ANBLMS>2.0.CO;2.

504 Long, C. S., and L. L. Stowe (1994), Using the NOAA/AVHRR to study
505 stratospheric aerosol optical thicknesses following the Mt. Pinatubo Eruption,
506 *Geophys Res Lett*, *21*, 2215–2218.

507 Louis, J., M. Tiedtke, and J. Geleyn (1982), A short history of the PBL
508 parameterization at ECMWF, in *ECMWF Workshop on Planetary Boundary Layer*
509 *Parameterization*, pp. 59–80, Reading, United Kingdom.

510 Marshall, G. J. (2003), Trends in the Southern Annular Mode from Observations and
511 Reanalyses, *J. Clim.*, *16*, 4134–4143, doi:10.1175/1520-
512 0442(2003)016<4134:TITSAM>2.0.CO;2.

513 McCormick, M., L. W. Thomason, and C. R. Trepte (1995), Atmospheric effects of
514 the Mt Pinatubo eruption, *Nature*, *373*, 399–404.

515 McCormick, M. P., and R. E. Veiga (1992), SAGE-II measurements of early
516 Pinatubo aerosols, *Geophys Res Lett*, *19*(2), 155–158.

517 McCormick, M. P., and T. J. Swissler (1983), Stratospheric aerosol mass and
518 latitudinal distribution of the el Chichon eruption cloud for October 1982, *Geophys*
519 *Res Lett*, *10*(9), 877–880, doi:10.1029/GL010i009p00877.

520 Moorthi, S., and M. J. Suarez (1992), Relaxed Arakawa-Schubert. A

521 Parameterization of Moist Convection for General Circulation Models, *Mon. Wea.*
522 *Rev.*, *120*, 978–1002.

523 Nagai, T., B. Liley, T. Sakai, T. Shibata, and O. Uchino (2010), Post-Pinatubo
524 Evolution and Subsequent Trend of the Stratospheric Aerosol Layer Observed by
525 Mid-Latitude Lidars in Both Hemispheres, *Sola*, *6*, 69–72, doi:10.2151/sola.2010-
526 018.

527 Niemeier, U., C. Timmreck, H. F. Graf, S. Kinne, S. Rast, and S. Self (2009), Initial
528 fate of fine ash and sulfur from large volcanic eruptions, *Atmos Chem Phys*, *9*(22),
529 9043–9057.

530 Pawson, S., R. S. Stolarski, A. R. Douglass, P. A. Newman, J. E. Nielsen, S. M.
531 Frith, and M. L. Gupta (2008), Goddard Earth Observing System chemistry-climate
532 model simulations of stratospheric ozone-temperature coupling between 1950 and
533 2005, *J. Geophys. Res.*, *113*(D12), D12103, doi:10.1029/2007JD009511.

534 Petters, M. D., and S. M. Kreidenweis (2007), A single parameter representation of
535 hygroscopic growth and cloud condensation nucleus activity, *Atmos Chem Phys*,
536 *7*(8), 1961–1971.

537 Randel, W. J., J. C. Gille, A. E. Roche, J. B. Kumer, J. L. Mergenthaler, J. W.
538 Waters, E. F. Fishbein, and W. A. Lahoz (1993), Stratospheric transport from the
539 tropics to middle latitudes by planetary-wave mixing, *Nature*, *365*, 533–535.

540 Read, W. G., L. Froidevaux, and J. W. Waters (1993), Microwave limb sounder
541 measurement of stratospheric SO_2 from the Mt. Pinatubo volcano, *Geophys Res Lett*,

542 *20*(12), 1299–1302.

543 Rienecker, M. M. et al. (2008), *The GEOS-5 Data Assimilation System—*
544 *Documentation of Versions 5.0.1, 5.1.0, and 5.2.0*, NASA.

545 Rienecker, M. M. et al. (2011), MERRA: NASA's Modern-Era Retrospective
546 Analysis for Research and Applications, *J Climate*, *24*(14), 3624–3648,
547 doi:10.1175/JCLI-D-11-00015.1.

548 Robock, A. (2000), Volcanic eruptions and climate, *Rev Geophys*, *38*(2), 191–219.

549 Robock, A., T. Adams, M. Moore, L. Oman, and G. Stenchikov (2007), Southern
550 Hemisphere atmospheric circulation effects of the 1991 Mount Pinatubo eruption,
551 *Geophys Res Lett*, *34*(23), doi:10.1029/2007GL031403.

552 Roscoe, H. K., and J. D. Haigh (2007), Influences of ozone depletion, the solar cycle
553 and the QBO on the Southern Annular Mode, *Q J Roy Meteor Soc*, *133*(628), 1855–
554 1864, doi:10.1002/qj.153.

555 Russell, P. et al. (1996), Global to microscale evolution of the Pinatubo volcanic
556 aerosol derived from diverse measurements and analyses, *J Geophys Res-Atmos*,
557 *101*(D13), 18745–18763.

558 Stenchikov, G., I. Kirchner, A. Robock, H. Graf, J. Antuña, R. Grainger, A. Lambert,
559 and L. Thomason (1998), Radiative forcing from the 1991 Mount Pinatubo volcanic
560 eruption, *J Geophys Res-Atmos*, *103*(D12), 13837–13857.

561 Stieglitz, M., A. Ducharne, R. Koster, and M. Suarez (2001), The Impact of Detailed

562 Snow Physics on the Simulation of Snow Cover and Subsurface Thermodynamics at
563 Continental Scales, *J. Hydrometeor*, *2*(3), 228–242.

564 Thomas, M. A., C. Timmreck, M. A. Giorgetta, H. F. Graf, and G. Stenchikov
565 (2009a), Simulation of the climate impact of Mt. Pinatubo eruption using ECHAM5-
566 Part 1: Sensitivity to the modes of atmospheric circulation and boundary conditions,
567 *Atmos Chem Phys*, *9*(2), 757–769.

568 Thomas, M. A., M. A. Giorgetta, C. Timmreck, H. F. Graf, and G. Stenchikov
569 (2009b), Simulation of the climate impact of Mt. Pinatubo eruption using ECHAM5-
570 Part 2: Sensitivity to the phase of the QBO and ENSO, *Atmos Chem Phys*, *9*(9),
571 3001–3009.

572 Thomason, L. W., L. R. Poole, and T. Deshler (1997), A global climatology of
573 stratospheric aerosol surface area density deduced from Stratospheric Aerosol and
574 Gas Experiment II measurements: 1984–1994, *J. Geophys. Res.*, *102*(D7), 8967–
575 8976, doi:10.1029/96JD02962.

576 Timmreck, C., H. Graf, and I. Kirchner (1999a), A one and half year interactive
577 MA/ECHAM4 simulation of Mount Pinatubo Aerosol, *J. Geophys. Res.*, *104*, 9337–
578 9359.

579 Timmreck, C., H. Graf, and J. Feichter (1999b), Simulation of Mt. Pinatubo volcanic
580 aerosol with the Hamburg climate model ECHAM4, *Theoretical and Applied*
581 *Climatology*.

582 Trepte, C. R., R. E. Veiga, and M. P. McCormick (1993), The Poleward Dispersal of

583 Mount-Pinatubo Volcanic Aerosol, *J. Geophys. Res.*, *98*(D10), 18563–18573.

584 Vernier, J. P. et al. (2011), Major influence of tropical volcanic eruptions on the
585 stratospheric aerosol layer during the last decade, *Geophys Res Lett*, *38*(12),
586 doi:10.1029/2011GL047563.

587 Young, R. E., H. Houben, and O. B. Toon (1994), Radiatively forced dispersion of
588 the Mt. Pinatubo volcanic cloud and induced temperature perturbations in the
589 stratosphere during the first few months following the eruptions, *Geophys Res Lett*,
590 *21*(5), 369–372.

591 Zhao, J., R. P. Turco, and O. B. Toon (1995), A model simulation of Pinatubo
592 volcanic aerosols in the stratosphere, *J. Geophys. Res.*

593

594

Figure captions

Figure 1: Global mean of the visible aerosol optical thickness as simulated by GEOS-5 and as derived by SAGE II and AVHRR data. Background values have been removed from the AVHRR data. The shaded area shows the variability of the ensemble.

Figure 2: Zonal mean of the aerosol optical thickness at 550 nm for the Mt. Pinatubo eruption in the GEOS-5 simulations, SAGE-II and AVHRR observations. Background values have been removed from the AVHRR observations.

Figure 3: Vertical profile of the monthly average of the SO_2 mixing ratio in the latitudinal band between 10°S and 10°N. The black solid line represents the ensemble average and the shaded area the variability of the ensemble. The diamonds are MLS measurements by [*Read et al.*, 1993].

Figure 4: Zonal mean of the SO_4 concentration from Mt. Pinatubo on July 15th, September 1st, November 1st and December 31st, 1991.

Figure 5: Horizontal distribution of SO_4 column mass between 30 hPa and the top of the atmosphere on July 2nd, 1991 and on July 16th, 1991.

Figure 6: Temporal evolution of the zonally averaged aerosol optical thickness at 550 nm in the ensembles with no radiatively interactive aerosol and SO_2 injection height between 16 and 18 km (upper panel) and 17 and 27 km (lower panel).

614 Figure 7: December 1991 monthly mean of the zonally averaged SO_4
615 concentration in the reference simulation (left panel), in the non interactive
616 simulation with SO_2 injection height between 16 km and 18 km (middle panel) and in
617 the non interactive simulation with SO_2 injection height between 17 km and 27 km
618 (right panel).

619 Figure 8: Streamlines of the difference between the horizontal wind field in
620 the interactive and in the non-interactive simulation on June 16th, 1991 (upper panel)
621 and on July 1st, 1991 (lower panel) at 70 hPa and 30 hPa altitude, respectively. The
622 shaded areas show the heating rates of sulfate from the eruption of Mt. Pinatubo due
623 to the interaction with longwave radiation.

624 Figure 9: Horizontal distribution of the SO_4 concentration in the reference
625 simulation and streamlines of the difference of the horizontal wind between the
626 reference simulation and the simulation without interactive aerosol at 30 hPa (upper
627 panel) and 100 hPa (lower panel) on June 24th, 1991.

628 Figure 10: Difference of the vertical velocity in mm/s between interactive and
629 non-interactive case at 70 hPa on June 16th, 1991 and at 30 hPa on July 1st, 1991
630 (shaded areas). The contours mark the concentration of SO_4, in $\mu g/m^3$. The average is
631 calculated over 5 ensemble members, since the needed diagnostic was not available
632 for all the eight ensemble members.

633 Figure 11: Zonal mean of the SO_4 concentration on October 15th, 1991 in the
634 simulations with low volcanic burden. In these experiments we injected 5 Tg of SO_2
635 between 16 and 18 km (left panel) and between 17 and 27 km (right panel), at the

same time and location of the Mt. Pinatubo eruption.

637

Ensemble member	*e*-folding time	
	SO_2	SO_4
1st	31	373
2nd	29	340
3rd	26	243
4th	34	426
5th	29	372
6th	29	345
7th	26	275
8th	34	402
Average	29.8	347
Standard deviation	2.9	57.7

638 Table 1: SO_2 and SO_4 *e*-folding time of each ensemble member included in

639 this study, and average values and standard deviation of the ensemble.

640

640

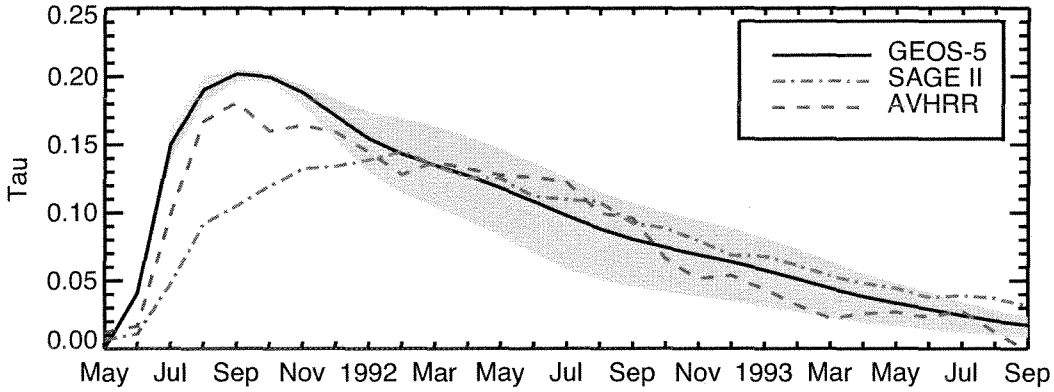

641

642 Figure 1: Global mean of the visible aerosol optical thickness as simulated by
643 GEOS-5 and as derived by SAGE II and AVHRR data. Background values have
644 been removed from the AVHRR data. The shaded area shows the variability of the
645 ensemble.

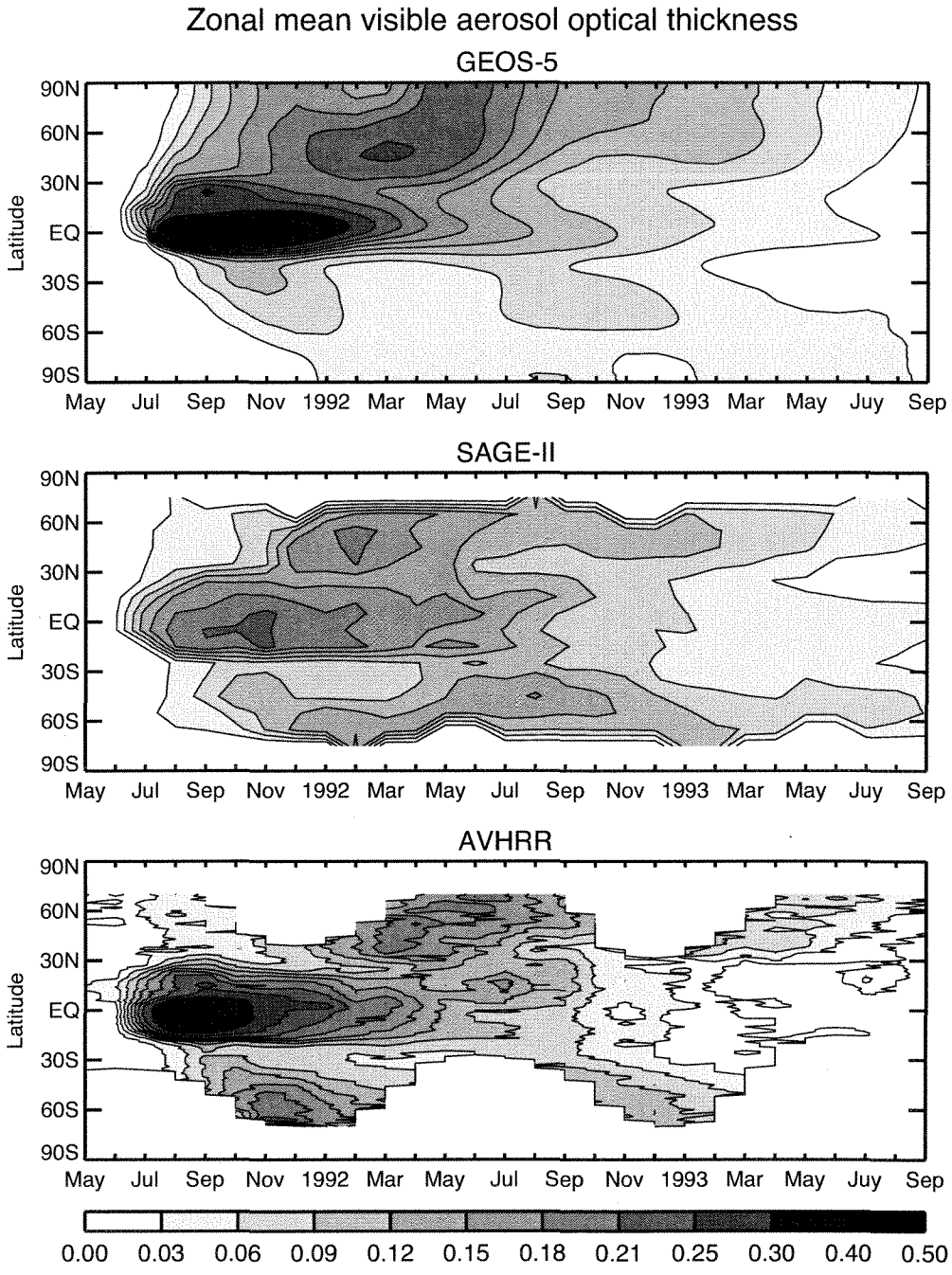

646

647 Figure 2: Zonal mean of the aerosol optical thickness at 550 nm for the Mt.

648 Pinatubo eruption in the GEOS-5 simulations, SAGE-II and AVHRR observations.

649 Background values have been removed from the AVHRR observations.

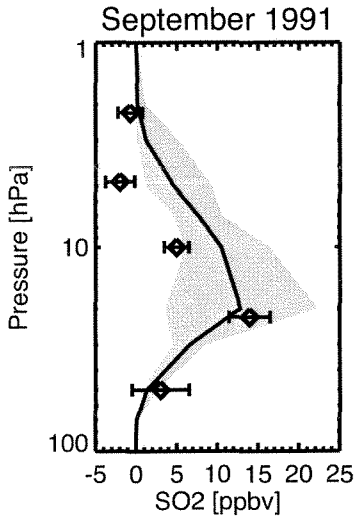

650

651 **Figure 3: Vertical profile of the monthly average of the SO_2 mixing ratio in**
652 **the latitudinal band between 10˚S and 10˚N. The black solid line represents the**
653 **ensemble average and the shaded area the variability of the ensemble. The**
654 **diamonds are MLS measurements by [*Read et al.*, 1993].**

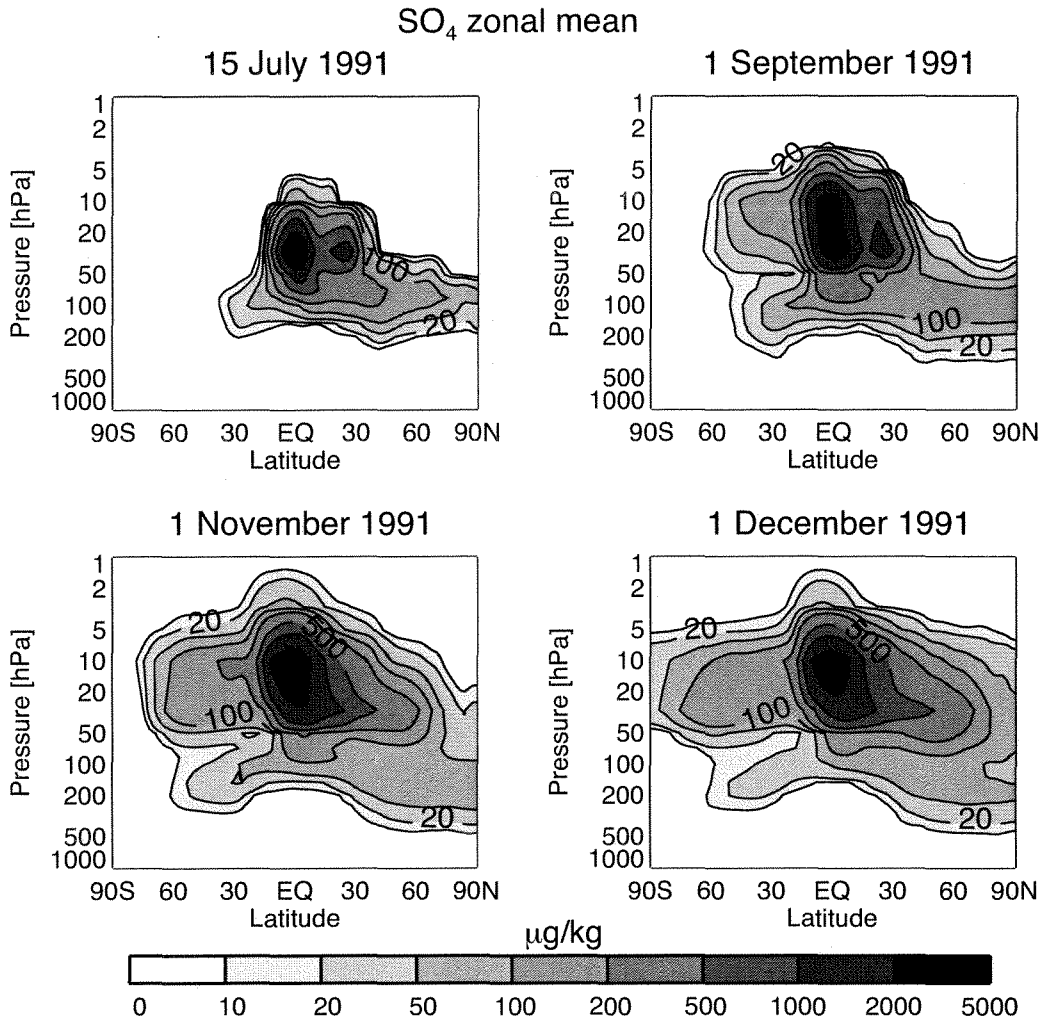

655

656 **Figure 4: Zonal mean of the SO_4 concentration from Mt. Pinatubo on July**

657 **15th, September 1st, November 1st and December 31st, 1991.**

658

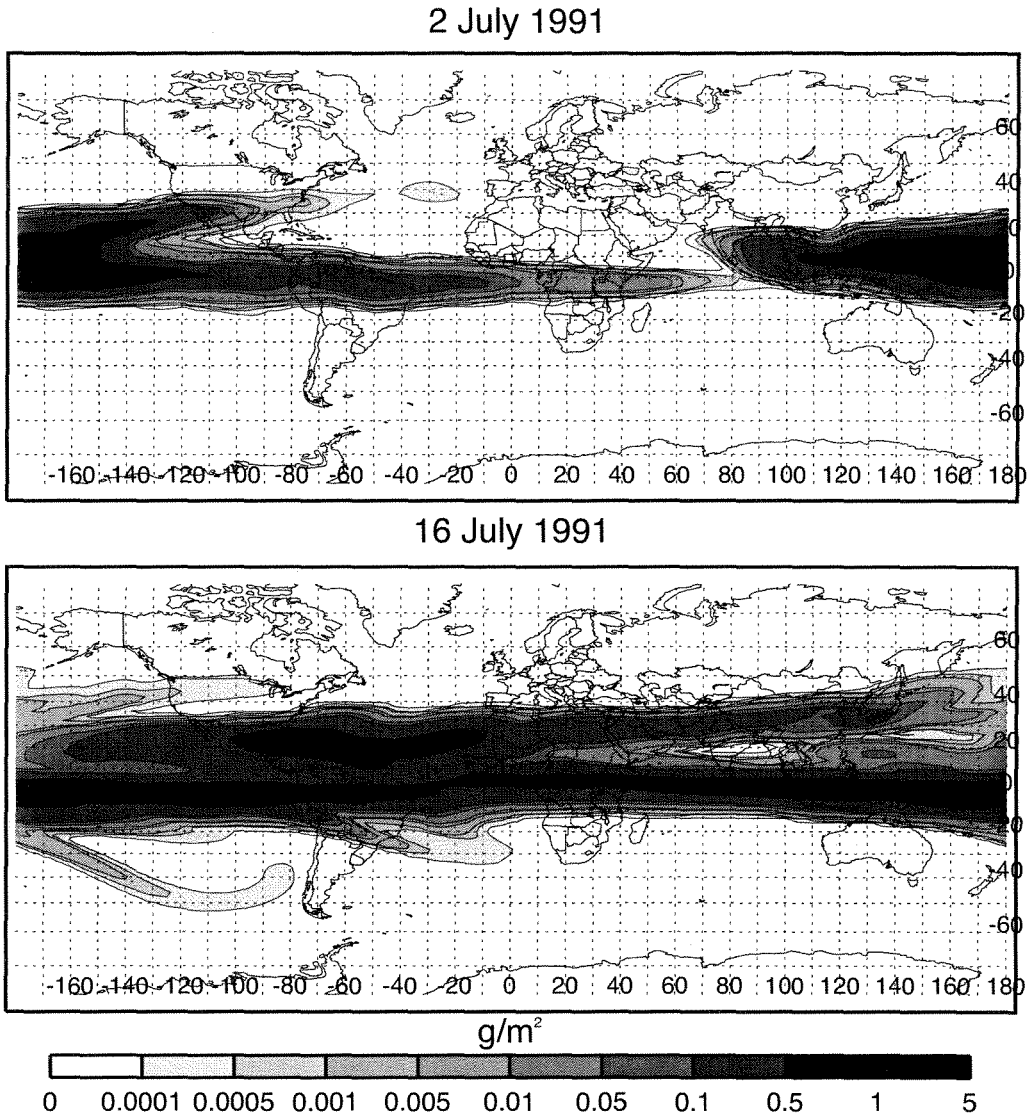

658

659 **Figure 5: Horizontal distribution of SO_4 column mass between 30 hPa and**

660 **the top of the atmosphere on July 2nd, 1991 and on July 16th, 1991.**

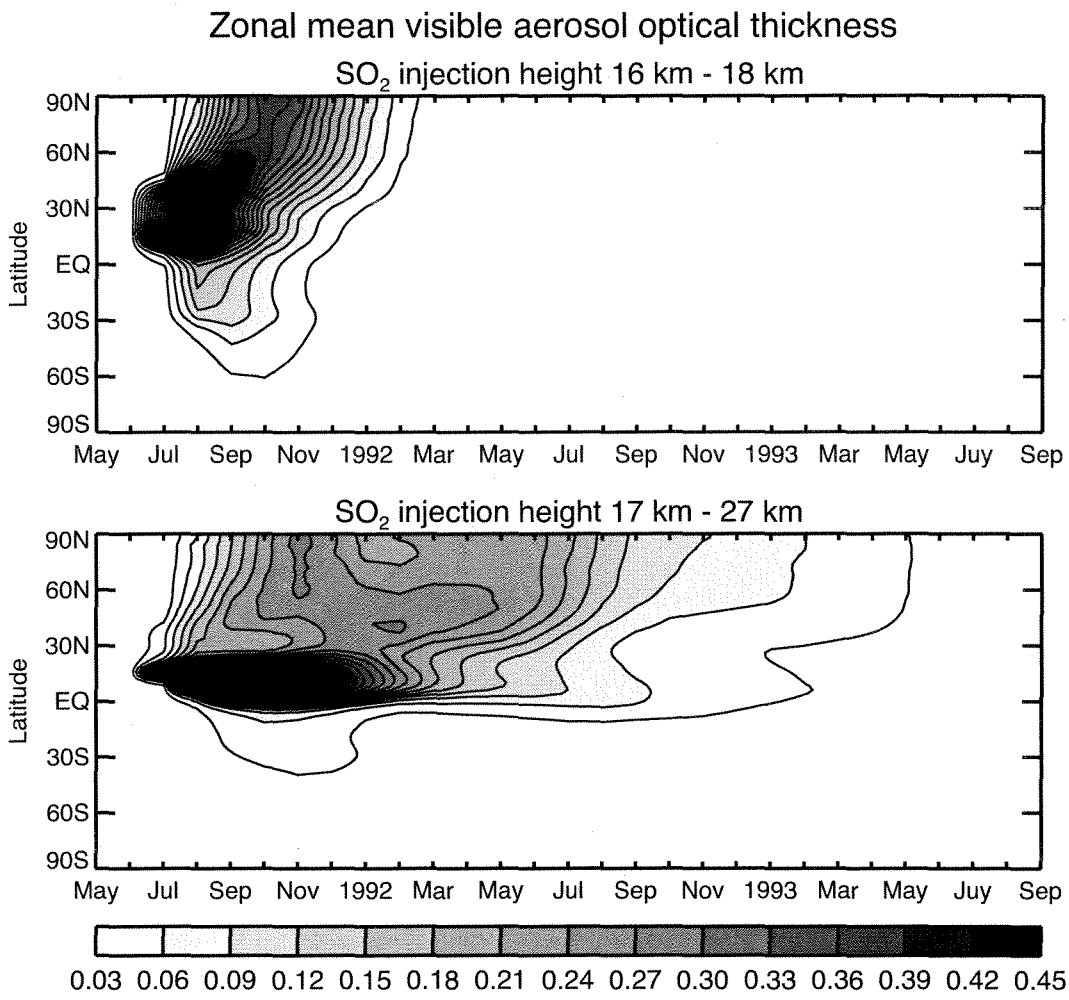

661

662 **Figure 6: Temporal evolution of the zonally averaged aerosol optical**

663 **thickness at 550 nm in the ensembles with no radiatively interactive aerosol and SO_2**

664 **injection height between 16 and 18 km (upper panel) and 17 and 27 km (lower**

665 **panel).**

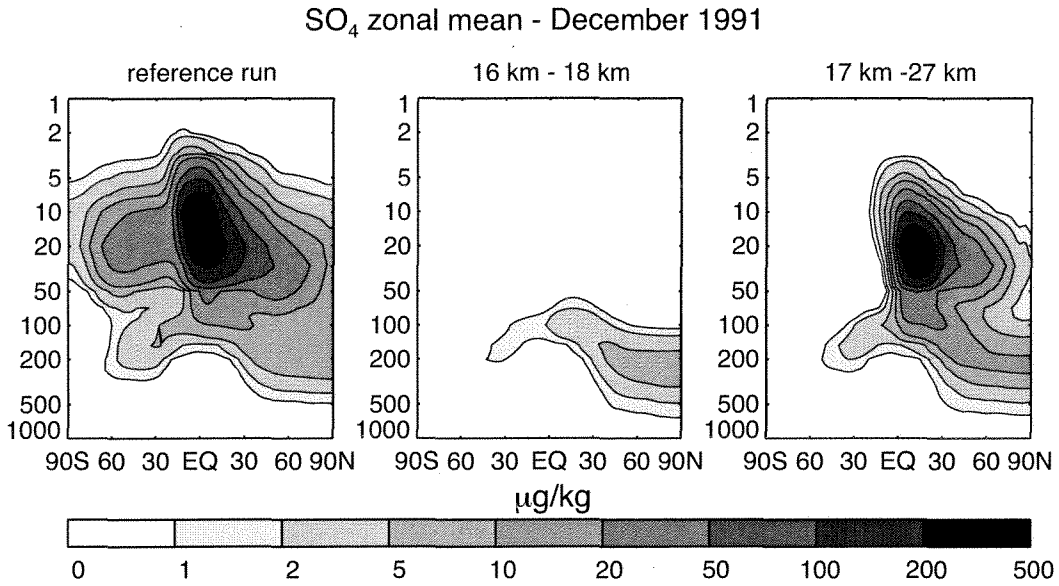

666

667 Figure 7: December 1991 monthly mean of the zonally averaged SO_4

668 concentration in the reference simulation (left panel), in the non interactive

669 simulation with SO_2 injection height between 16 km and 18 km (middle panel) and

670 in the non interactive simulation with SO_2 injection height between 17 km and 27

671 km (right panel).

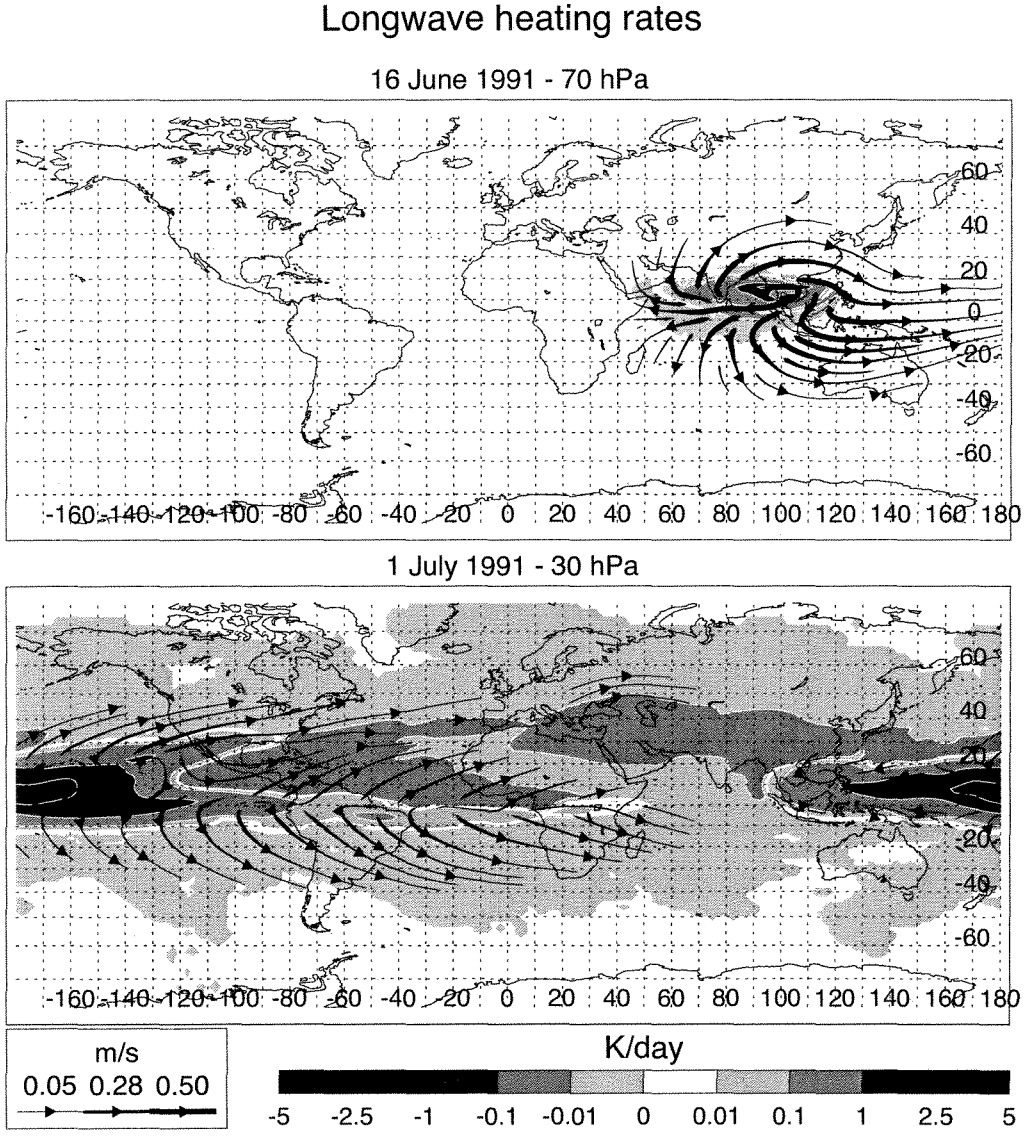

672

673 **Figure 8: Streamlines of the difference between the horizontal wind field in**

674 **the interactive and in the non-interactive simulation on June 16th, 1991 (upper**

675 **panel) and on July 1st, 1991 (lower panel) at 70 hPa and 30 hPa altitude,**

676 **respectively. The shaded areas show the heating rates of sulfate from the eruption of**

677 **Mt. Pinatubo due to the interaction with longwave radiation.**

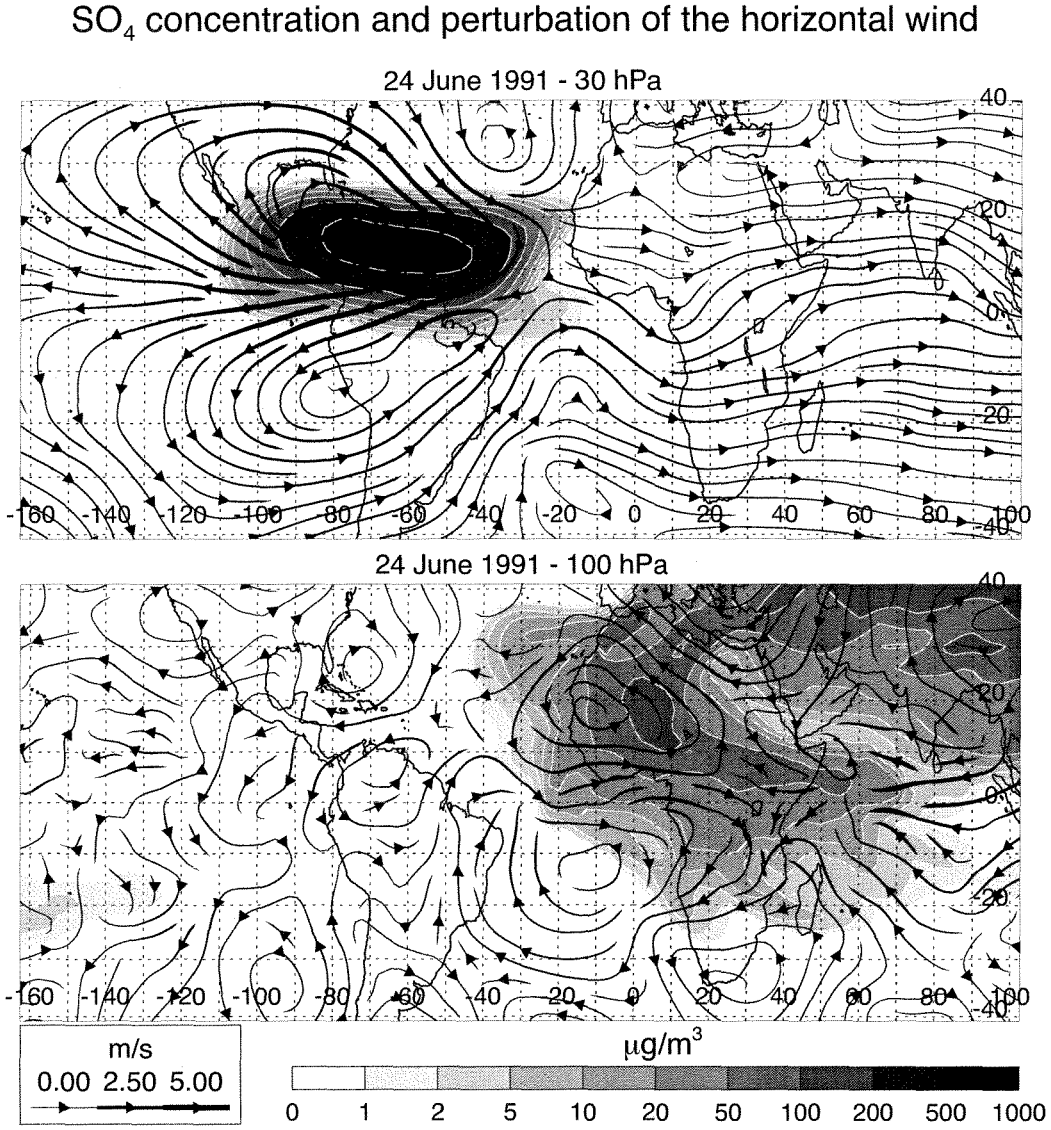

678

679 **Figure 9: Horizontal distribution of the SO_4 concentration in the reference**

680 **simulation and streamlines of the difference of the horizontal wind between the**

681 **reference simulation and the simulation without interactive aerosol at 30 hPa (upper**

682 **panel) and 100 hPa (lower panel) on June 24th, 1991.**

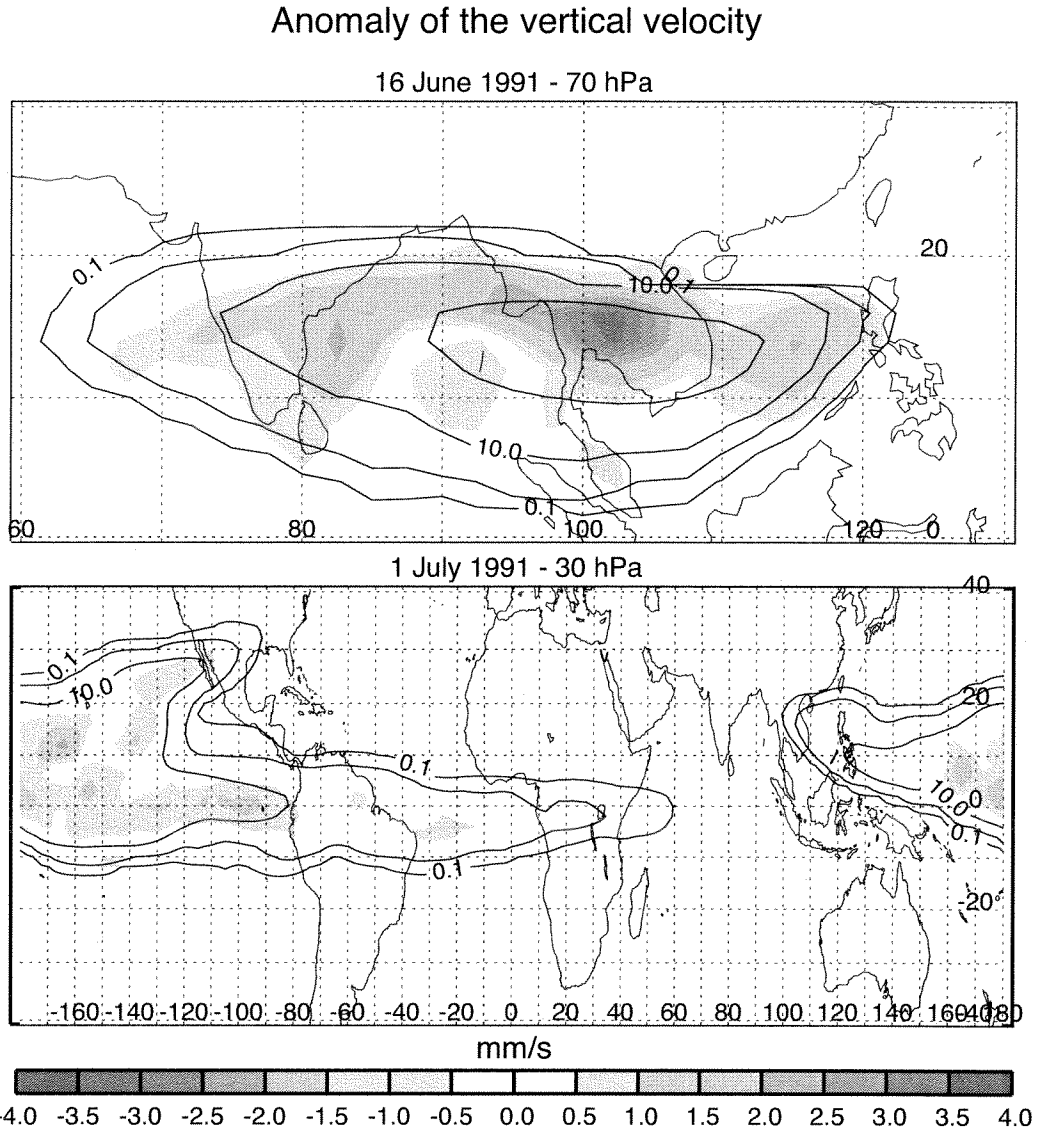

Figure 10: Difference of the vertical velocity in mm/s between interactive and non-interactive case at 70 hPa on June 16th, 1991 and at 30 hPa on July 1st, 1991 (shaded areas). The contours mark the concentration of SO_4, in $\mu g/m^3$. The average is calculated over 5 ensemble members, since the needed diagnostic was not available for all the eight ensemble members.

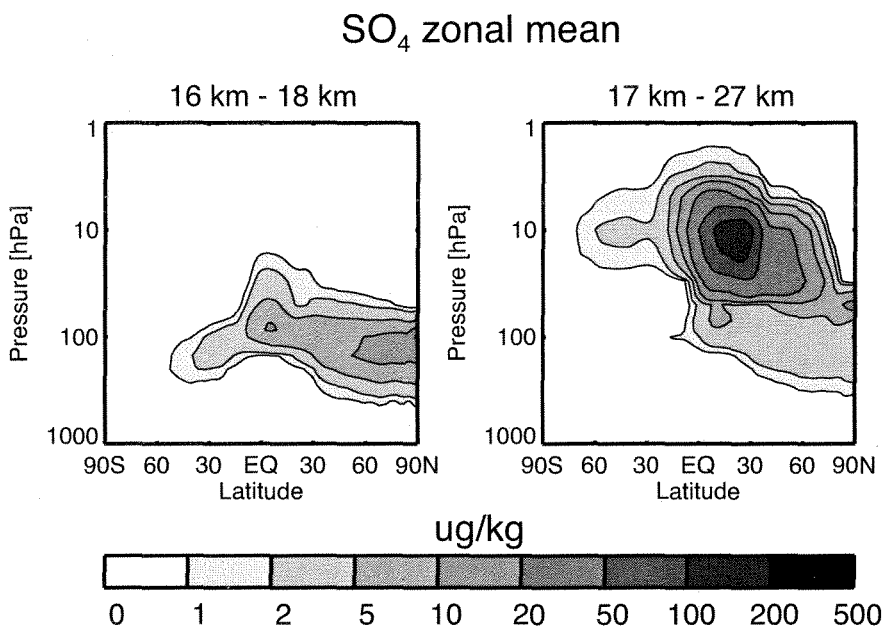

689

690 **Figure 11: Zonal mean of the SO_4 concentration on October 15th, 1991 in the**

691 **simulations with low volcanic burden. In these experiments we injected 5 Tg of SO_2**

692 **between 16 and 18 km (left panel) and between 17 and 27 km (right panel), at the**

693 **same time and location of the Mt. Pinatubo eruption.**